Chapter 4

Results

Although this thesis is mainly focused on the detection and classification of apparent extremely red galaxies, we use our large data set to look also at the overall J-band selected galaxy population and its distribution in the R-J *vs.* J colour plane.

4.1 J-band galaxy counts

Galaxy number counts and the colours of galaxies making up those counts have proved to be a powerful tool for investigating cosmological geometry (Peebles 1993) and galaxy evolution. Observations made at a wide range of magnitudes and wavelengths can, in principle, distinguish between different cosmological and evolutionary models. Using a single passband introduces different selection effects, which is not necessarily a disadvantage as long as the selection function is well understood. Indeed, these selection effects can be used deliberately for probing different galaxy populations and different aspects of their evolution.
While selection in blue passbands is used to study star-forming sources, selection in the near infrared is predominantly sensitive to the light of older stellar populations.

Near IR k-corrections are small even at redshifts above unity, and insensitive to the spectral type of the observed objects (Cowie et al. 1994) and to short lived bursts of star formation (Kauffmann and Charlot 1998).
Therefore, near-infrared surveys are much less biased with respect to the mix of spectral types compared to optical selected surveys. In addition, the uncertainties due to inhomogeneous dust absorption are reduced in the near-infrared.

There are numerous K-band galaxy surveys, such as the K20 survey of Cimatti et al. (2002b), the Munich Near-Infrared Cluster Survey (MUNICS, Drory et al. 2001), the HAWAII K-band galaxy survey (Huang et al. 1997) and the Two Micron All Sky Survey (2MASS, Skrutskie et al. 1995).
However, the number of J-band surveys is relatively small and lacks sky coverage. Bershady, Lowenthal & Koo (1998) and Saracco (1999) have published deep J counts; other surveys extend the magnitude range to $13<J<20$, e.g. MUNICS (Drory et al. 2001, Väisänen et al. 2000). Our survey covers an similar magnitude range, but covers a 4 times larger area. Section 4.1.2 describes how our results compare to other surveys.

Figure 4.1 and Table 4.1 summarise the results for the J-band galaxy number counts from our survey. The best fit slope for our J-counts (α = d log[N(J)] / dJ) was derived in two magnitude intervals:

- $12.50^{mag} \leq$ J $<$ 17.25: $\alpha = 0.54 \pm 0.01$
- $17.25^{mag} \leq$ J $<$ 19.00: $\alpha = 0.33 \pm 0.04$.

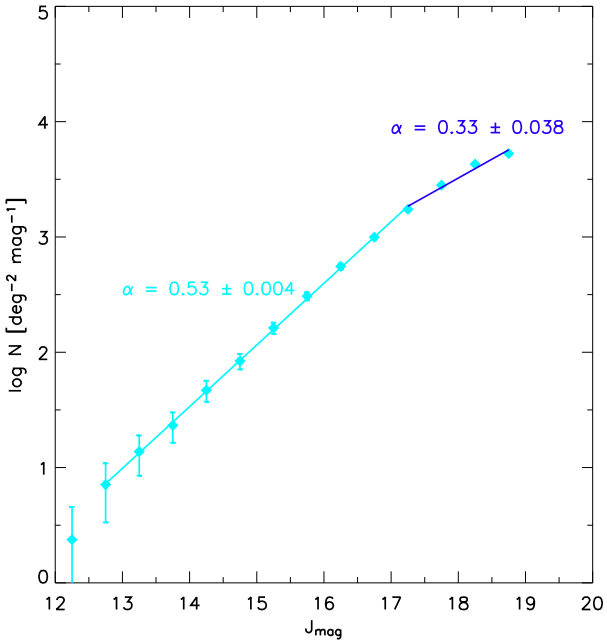

Figure 4.1: The observed differential number counts in our survey. The error bars indicate the Poisson uncertainties. The number counts have not been corrected for incompleteness. Note that compared to other surveys with only one or a few contiguous fields, the large number of disjoint fields largely eliminates large scale structure as a source of uncertainty.

However, the flattening at faint J magnitudes might be the result of different incompleteness limits for each individual field, which in turn depend on the photometric conditions which change with observing runs. The estimates for the detection limit of stars (J=18.75) and random magnitude errors are based on simulations for one field and should be considered as rough estimate.

J - Magnitude	N [deg^{-2} mag^{-1}]	log N	log N$_{low}$	log N$_{up}$
12.25	2.3	0.0738	-0.7143	0.6577
12.75	7.1	0.8519	0.5237	1.0367
13.25	13.7	1.1383	0.9296	1.2785
13.75	23.2	1.3660	1.2152	1.4777
14.25	46.9	1.6715	1.5710	1.7529
14.75	83.9	1.9238	1.8509	1.9861
15.25	162.6	2.2111	2.1600	2.2568
15.75	306.7	2.4867	2.4501	2.5204
16.25	555.1	2.7444	2.7175	2.7697
16.75	995.0	2.9978	2.9779	3.0169
17.25	1737.5	3.2399	3.2249	3.2544
17.75	2815.0	3.4495	3.4377	3.4609
18.25	4277.6	3.6312	3.6217	3.6404
18.75	5286.4	3.7231	3.7146	3.7315
19.25	3912.1	3.5925	3.5824	3.6021

Table 4.1: Differential galaxy number counts in the total survey. The counting was done in 0.5 mag bins, but has been rescaled to a per-magnitude quantity.

4.1.1 Uncertainties in the number counts

Several factors contribute to the uncertainty in the galaxy number counts; such as the Poisson noise, the clustered galaxy distribution, and magnitude errors and uncertainties in the star-galaxy separation. As we demonstrated in section 2.3.1, the latter effect is negligible: the star-galaxy separation is very robust over the whole magnitude range for which stars can be detected.
As noted by Huang et al. (1997), uncertainties due to large-scale structures, such as rich clusters and voids, are hard to quantify. Indeed, these might be a reason for the varying results in galaxy counts (see chapter 4.1.2). The effect of systematic magnitude errors on the final number counts can be estimated from equation 4.1 (see Huang et al. 1997):

$$\alpha\sigma_s \quad = \quad \frac{\sigma}{N(m)} \tag{4.1}$$

where α is the slope of the number count distribution, σ is the final uncertainty for the number of counts per magnitude per square degree in all fields, and σ_s is the systematic error.

In our case, the systematic error is the error in zero point, which in J-band was σ_s= 0.07 between observing runs. This error does not change the slope of log N (Figure 4.1, but it shifts the log N in horizontal direction in the count-magnitude diagram. If we take the slope of 0.53 and σ_s= 0.07, we obtain σ/N = 3.8%.

Random error in the magnitude can also change log N. In the J-band, the sky background is much higher than the galaxy flux. Hence, the random error in the magnitude of galaxies is mainly caused by the sky background. The observed profile of the galaxy number counts as a function of magnitude is a result of the real log N profile of the counts, convolved with the random error distribution function, which is usually a Gaussian distribution.
Since both random errors and galaxy number counts increase with fainter magnitudes, on average there are more faint galaxies appearing falsely in a certain bin than brighter galaxies. The observed slope of log N therefore becomes steeper than the real one.
Considering that only the galaxies at adjacent bins can contribute erroneously to the galaxy counts, Huang et al. (1997) estimate the change in slope to be :

$$\Delta\alpha \quad = \quad 1.15\alpha^2 \ \frac{\sigma_{r1}^2-\sigma_{r2}^2}{m_1-m_2} \ . \tag{4.2}$$

Using the random error estimates from Figure 2.19, $\sigma_{r1} = 0.1^{mag}$ at $m_1 = 15^{mag}$ and σ_{r2} = -0.4 at m_2 = 18, and α=0.53, we obtain $\Delta\alpha$ = 0.016 at J=18. Compared to the 1 σ error of the slope, $\Delta\alpha_f$ = 0.004, this error dominates the accuracy of the slope of log N, but does not change its absolute value significantly.

4.1.2 Comparison with other surveys

The number counts shown in Figure 4.2 agree well with the values counts of Drory et at. (2001) and Väisänen (2000), although they are somewhat higher than the Saracco et al. (1999) and Martini (2001) counts.
The Sarraco at al. (1999) survey extends much fainter galaxies than does ours, and the two

surveys overlap only at our faintest magnitudes. In this range, the calculated surface density is affected by the small number statistics. All the J-band counts in the range 13 - 18 mag have essentially the same slope as our data, $\alpha \approx 0.53$. Also the flattening at the faint end, agrees with the result of Saracco et al. (1999) and Bershady et al. (1998), who found slopes of ≈0.35 and 0.34, respectively.
However, the observed differences can partially explained by different definitions of the J magnitude, e.g IRAF aperture magnitude or SExtractor magnitude.

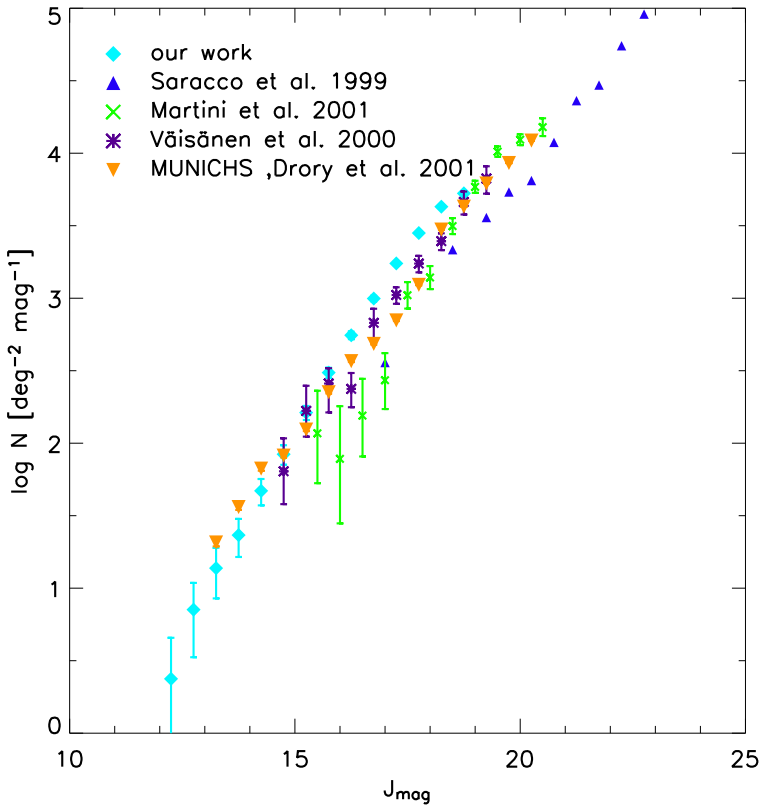

Figure 4.2: Differential counts (number mag^{-1} deg^{-2}) of galaxies in the J-band compared to a collection of published data, including Sarraco et al. (1999), Martini (2001), Väisänen et al. (2000) and the MUNICS survey (Drory et al. 2001). The error bars for our data represent only counting statistics.

4.2 Colour - magnitude distribution

Figure 4.3 shows the distribution of colours for all galaxies (in both R and J band) between 15 $\leq$ J $\leq$ 21, from which the mean R-J colour and FWHM in different J magnitude intervals have been calculated (see Table 4.2). Note, that contrary to the ERO candidates, the overall galaxy sample (with over 58000 sources) has not been thoroughly checked for remaining bad pixels, or otherwise false detections. Nevertheless, by excluding the outer 300 pixel of the final mo-

saic (2300 x 2300 pixels) from the detection area, we avoid a larger number of false detections.

The mean colour in the intervals from <J>∼14.5 to up to <J>∼ 19.5 increases by 1.55 magnitudes from R-J = 1.70 to R-J = 3.25. Such a trend was also observed by Daddi et al. (2000) and Thompson et al. (1999) for the mean R-K colours, which reach their maximum between K ∼ 18-19. This redward shift of the mean colour might result from a growing fraction of high-redshift galaxies.

The interval 18 ≤J <19 shows an especially interesting feature: the distribution shows clearly a second peak, which has not been described before and therefor requires special attention.
Comparing the colour distribution with the result without the substitution of the faintest R- magnitudes by the limiting magnitude, shows that this second, subsidiary peak at fainter magnitudes, is solely the result of this procedure.

J-magnitude	mean R-J colour	FWHM
$14 \leq J < 15$	1.70 ± 0.01	0.377 ± 0.013
$15 \leq J < 16$	1.75 ± 0.01	0.467 ± 0.021
$16 \leq J < 17$	1.81 ± 0.01	0.561 ± 0.021
$17 \leq J < 18$	1.94 ± 0.01	0.875 ± 0.033
$18 \leq J < 19$	2.97 ± 0.03	2.209 ± 0.032
	5.65 ± 0.19	1.482 ± 0.194
$19 \leq J < 20$	3.13 ± 0.02	1.707 ± 0.023

Table 4.2: The colour distribution of the total galaxy sample,

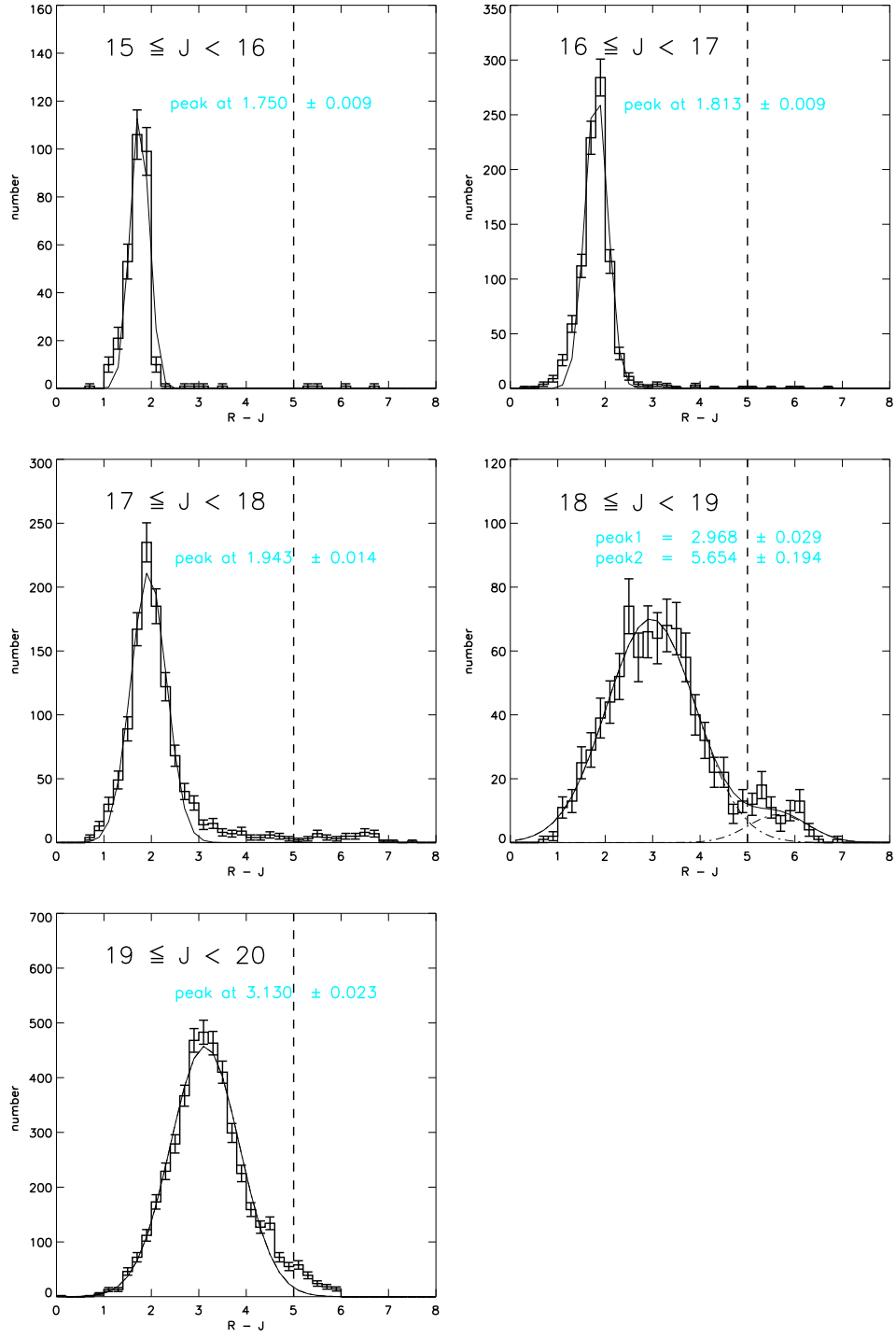

Figure 4.3: R-J colour distribution for all galaxies, i.e. stellarity index ≤0.8 in R and J-band. Magnitude ranges are indicated in the upper left-hand corner of each panel. The dashed line represents the R-J≥5 ERO criterion. The error bars indicate the Poisson uncertainties and the dot-dashed line in the panel 18 ≤ J < 19 show the two Gaussians used to fit the peak position and width of the distribution reported in Table 4.2. The second peak is the result of assigning the limiting R magnitude to objects with no optical detection (see text for details).

4.3 The abundance of extremely red galaxies

The final catalogue of extremely red objects contains 160 sources redder than R-J≥5 and brighter than J∼20. Figure 4.4 shows an example for an ERO with and without R-band detection. Approximately 55% of all EROs have a detection both in J and R-band and a stellarity ≤ 0.8, 30% are objects without R-band detection and 15% are objects fainter than J=18.75^{mag}. Although we used the stellarity index as a criterion to distinguish between stars and galaxies, the number of galaxies with no R-band detection has to be treated as an upper limit. Deeper optical photometry might identify a small fraction of these objects as stars.

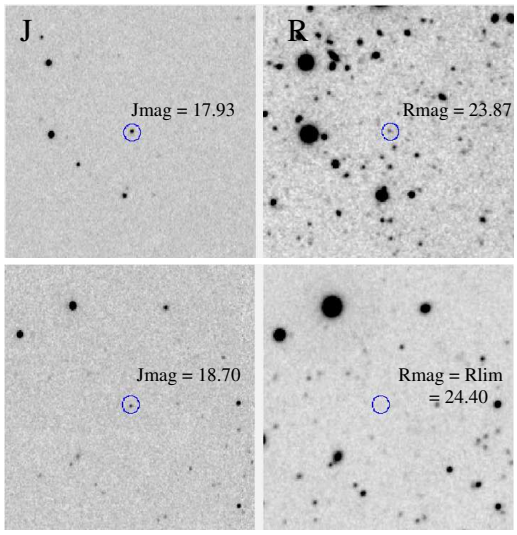

Figure 4.4: J- and R-band image of an ERO. The upper panel shows object G184_118, the lower panel G177_657. For detailed information, e.g coordinates and magnitudes see Appendix C.

4.3.1 Surface density of EROs

The integrated surface density of EROs is defined as the total number of EROs brighter than a given magnitude per unit unit area on the sky. In our 4.5 deg^2 we found 160 objects with R-J≥5, yielding a surface density of:

$$\Sigma = (0.97 \pm 0.07) \times 10^{-2}\ arcmin^{-2}\ \ with\ \ R-J \geq 5\ \ and\ J \lesssim\ 20.0.$$

The resulting cumulative surface density is shown in Figure 4.6 and Table 4.3. Comparing our results with those of other surveys is difficult, since all of them applied different colour criteria selecting different galaxy populations. The only other survey with a similar strong colour criteria is a small sub-sample from Daddi et al. (2000), selecting EROs with R-K≥7. According to stellar synthesis models (2004), these objects are also elliptical galaxies with an old stellar population. Daddi found 5 such objects within the completeness limit of their deep survey (K≤19.2, area = 447 arcmin^2). Keeping in mind that the Daddi sample has fainter near-infrared magnitudes, the resulting surface density of 0.011 arcmin $^{-2}$ is about the same

as our result.

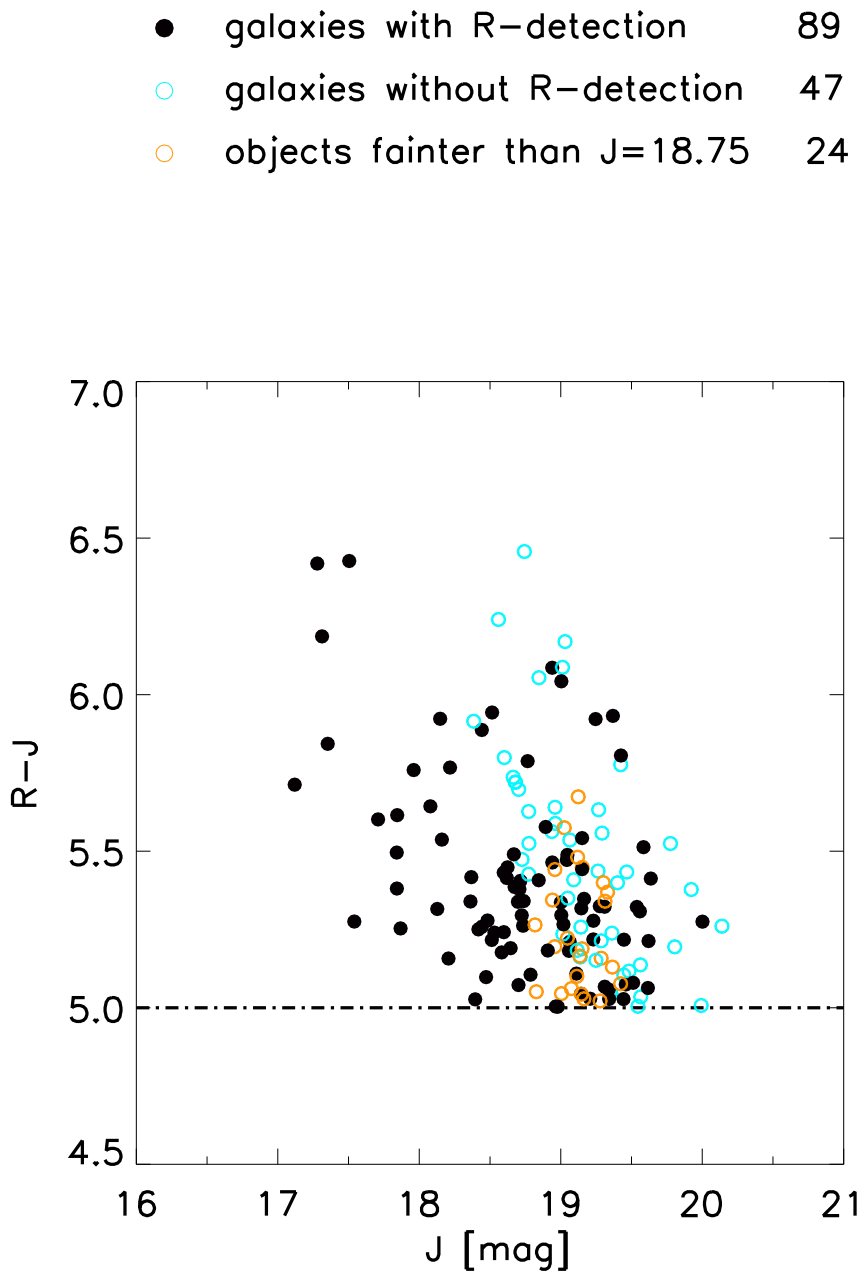

Figure 4.5: The colour-magnitude distribution of extremely red galaxies. The graph contains both objects which are classified as galaxies due to their *stellarity* index or because their J magnitude is fainter than 18.75. We would not expect to detect any stars fainter than this magnitude (see section 2.3.1).

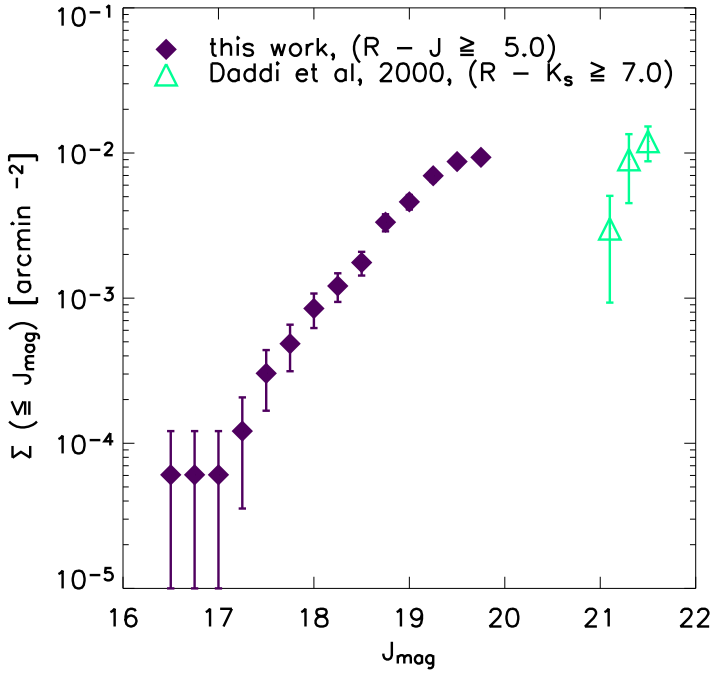

Figure 4.6: Integrated ERO surface density from this work, compared to the results for R-K≥7 from Daddi et al. 2000. The uncertainties are derived assuming only Poisson counting statistics. The Daddi J magnitudes are scaled, assuming J-K = 2.3.

J limits	N	N/arcmin^2
17.25	2	0.0001
17.50	5	0.0003
17.75	8	0.0004
18.00	14	0.0008
18.25	20	0.0012
18.50	29	0.0018
18.75	55	0.0033
19.00	76	0.0046
19.25	115	0.0070
19.50	144	0.0087
19.75	154	0.0093
20.00	158	0.0096
20.25	160	0.0098

Table 4.3: The number, N, of EROs, selected at limiting magnitude J and the cumulative surface density (in objects/arcmin^2). The counts contain both objects with and without R-band detections, as well as objects which are fainter than J=18.75

4.3.2 Estimates of the volume density

Although we have no redshift information for our sample, we can make a crude estimate of the volume density of EROs, based on the redshift range in which such objects can occur. The very red optical to near-infrared colour of an elliptical galaxy is the result of a strong 4000 Åbreak, shifted between the R and J-band. For elliptical galaxies with R-J $\geq$5, the SSP model (see section 3.4) predicts a lower limit for this redshift range of z$\approx$ 1.4.
The estimate for the upper limit is somewhat more difficult, since the result from stellar synthesis modelling depends on the assumed formation redshift. As an upper limit for our estimate, we have selected z=3, which seems rather high for objects which are that bright in J. The co-moving volume covered in this range, accumulated over all 79 fields in the assumed cosmology is $\sim 10^7$ Mpc ^{3}. For our sample of 160 EROs this yields a volume density of (1.615 $\pm$ 0.128) x 10^{-5} Mpc^{-3}. The error reflects only the low number statistics, and not the uncertainty in the volume estimate due to changes in the redshift limits. Using z=2 as upper limit, limiting the redshift range to $\sim$ $^1/_3$ of that for z$\sim$3, will decrease the co-moving volume to 4.6 x 10^6 Mpc^3 and increase the co-moving volume density by a factor of 2. EROs with R-K$\geq$6 (Thompson et al. 1999) have a similar volume density, averaged over an redshift range of 0.85$\leq$z$\leq$2.

Compared with quasars, this space density is a factor of 8 times higher. Boyle et al. (2000) found a space density of 2 $\times$ 10^{-6} Mpc^{-3} for quasars with $M_B \leq$ -23 in a similar redshift range. The results of stellar synthesis models (chapter 3) places the formation redshift at z>3, suggesting that massive structures have formed early in the universe.

4.3.3 Spatial distribution

Galaxies are not distributed randomly throughout the universe. Instead, nearly all galaxies are found in associations, either filaments, groups or clusters. How did the structure we see today form and develop? This question is one of the most challenging in today's study of cosmology. In order to address these question, we have to know the evolution of structure in detail. Several surveys have addressed the problem of structure formation and evolution by studying the galaxy distribution in different redshift intervals. In general, there are two ways to conduct such surveys, either large wide-angle surveys, which are limited to relative bright apparent magnitudes, and pencil-beam surveys, with small, but very deep, fields.

The most common approach to describe the structure of the matter distribution, is to investigate the angular-correlation function, $\omega(\theta)$. Daddi et at. (2000) first detected strong clustering of EROs. They found the angular correlation function of K$\leq$19.2 EROs (R-K$\geq$5) to be almost a factor ten higher than that of all galaxies to the same limit. Since local giant ellipticals are intrinsically much more clustered than disk galaxies (Guzzo et al. 1997), this was interpreted as evidence that most EROs are z>1 ellipticals.

In our survey we use a similar, approach to look for galaxy cluster candidates. From stellar synthesis models, we know that galaxies with R-J$\geq$5 are massive galaxies with evolved populations, whose stars formed at redshift 3 and above. Such galaxies are presumably in highly clustered environments, and since they are so massive will be close to the centre of the

cluster.
While the number of EROs per field is much too low to calculate any spatial correlation, we use the latter assumption to select a number of EROs as pointers to galaxy clusters at redshift 1.4 and above.
Figure 4.7 shows an example of a field with an almost 4 times higher surface density than the average, indicating overdensities on arcmin-scales. In the face of planned follow-up observations with high-resolution instruments, e.g. ISAAC (VLT) or the Advanced Camera for Surveys (ACS, HST) we have selected 19 fields of about 2.5 arcmin, which contain 2 or more EROs with R-J$\geq$5. Assuming a redshift of 2, such a field size corresponds to a physical scale of 1.27 Mpc. Two confirmed EROs (R-J$\geq$5, J$<$20 in a 2.5 arcmin field, have a 3 times higher surface density than EROs in the field.

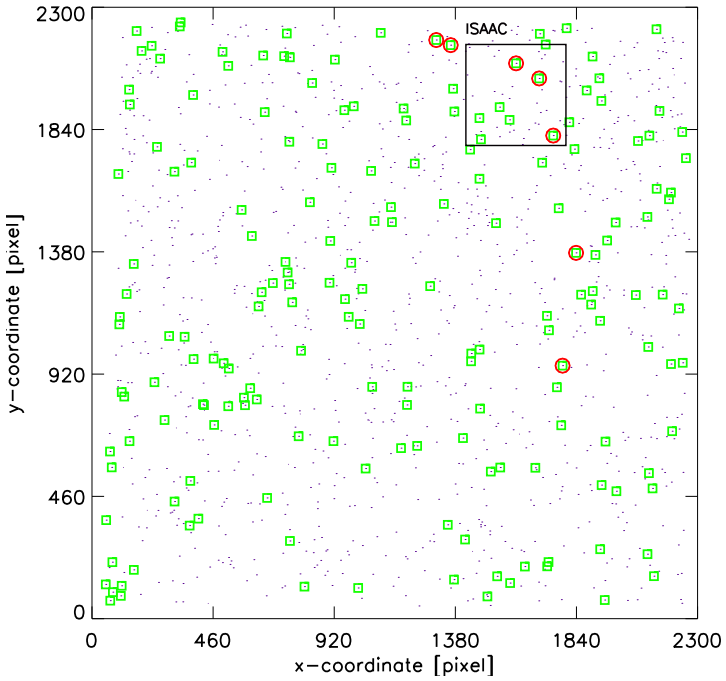

Figure 4.7: The spatial distribution of EROs (red circles) in field G126. The small field characterises the size of an ISAAC image, which represents an field of approximately 1.27 Mpc across, assuming $H_o = 70$, $\Omega_M = 0.3$ in a flat universe. The green symbols indicate objects with R-J$\geq$3.4, representing evolved ellipticals at z$\sim$1.